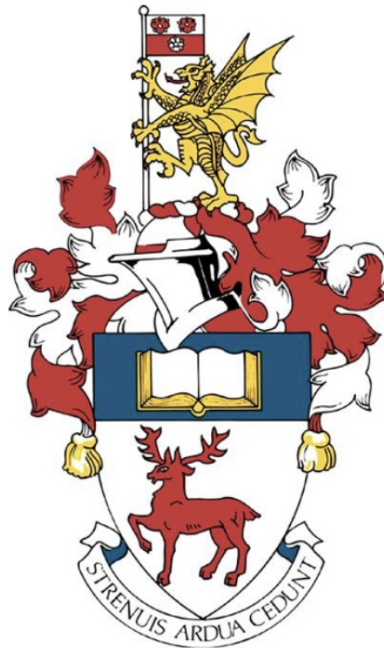


Modelling the Pause Phenomenon in X-ray Bursts from Low-Mass X-ray Binaries

Harry Charlesworth - 31851231
Supervisor, Diego Altamirano

May 11, 2025



Abstract

Energetic X-ray bursts arise from thermonuclear flashes from the surface of accreting neutron stars in low-mass X-ray binaries (LMXBs). These bursts typically exhibit a rapid rise in X-ray flux followed by a slower decay. The rise phase has historically been assumed to be smooth and continuous; however, recent observations have revealed a statistically significant pause, flattening in flux, during the initial rise.

In this work, we systematically investigate the prevalence of this pause feature by analysing a dataset of 124 X-ray bursts. Additionally, we evaluate and compare multiple modelling techniques tailored to the rise phase, to assess their effectiveness in identifying such features.

A filtering pipeline was used to systematically reject bursts based on evolving criteria. After initial filtering, 26 bursts were retained. Each burst was subsequently fitted six times using three distinct models (S-S-S, P-S-S, and S-S-P), each in both constrained and unconstrained form, to allow large scale statistics on model performance.

Time binning was standardized, and 14 fits across 10 bursts passed the final filtering criteria and were accepted for pause significance testing ($\geq 3\sigma$). Each fit was analysed alongside its counterparts generated at different time binning to assess the robustness of identified features.

Three bursts exhibited statistically significant pauses across all counterparts. The sources and measured durations were:

4U_0513-40 with a pause of **10.07 s \pm 0.38**

4U_1636-536 with a pause of **0.47 s \pm 0.053**

4U_1728-34 with a pause of **0.53 s \pm 0.014**

Of these, the pause detected in 4U_0513-40 was found to be extremely robust, with concerns regarding model dependence affecting the other two detections.

Acknowledgments

I would like to express my sincere gratitude to my supervisor, Diego Altamirano, for his invaluable support and guidance throughout this project. I am also grateful to Giulio Mancuso for his assistance with computational methods and for providing continuous technical support.

Contents

1	Introduction	4
2	Theoretical Background	5
2.1	Binary accretion physics	5
2.2	Physics of Neutron Stars and X-ray Bursts	6
3	Methods	11
3.1	Data Collection & Initial Filtering	11
3.2	Rise & Broad Plotting	12
3.3	Modelling Approaches	14
3.4	Final Set of Fits	16
3.5	Final Filtering	17
3.6	Statistical Significance Testing	19
4	Results	20
4.1	Model Comparison	20
4.2	Pause Significance	21
5	Discussion	28
5.1	Interpretation of Model Analysis	28
5.2	Interpretation of Significant Pauses	29
5.3	Pause comparison	30
5.4	Limitations	30
5.5	Implications for Future Research	30
6	Conclusion	31
A	Calculating L_{Edd} and \dot{m}_{Edd}	32
B	Key commands and explanations	32
C	1050010111, fitting data for S-S-S, P-S-S, and S-S-P	33

1 Introduction

Low-mass X-ray Binaries (LMXBs) describe systems in which a compact object, either a neutron star (NS) or a black hole (BH), accretes material from a low-mass companion star (typically, $< 1M_{\odot}$). Accretion occurs through Roche lobe overflow [1], where the companion star, having expanded during the later stages of stellar evolution, develops outer layers that exceed the boundary of its Roche lobe, and subsequently outer material falls under the gravitational influence of the compact object.

Material flowing from the companion star spirals towards the compact object forming an accretion disk where gravitational potential energy (GPE) is released as near-continuous X-ray emission. In the case of neutron stars the accreted material can build up on the surface until a sufficient pressure, and thus temperature, is reached at which point a thermonuclear flash occurs, resulting in an energetic X-ray burst. [2]

X-ray bursts are classified into two distinct types, a scheme first introduced by Hoffman, Marshall, and Lewin in 1978 [3]. Type I bursts arise from thermonuclear explosions on the surface of neutron stars triggered by the unstable burning of accreted hydrogen and helium. These bursts typically exhibit rise times of $\lesssim 1\text{--}10$ s and last tens to hundreds of seconds [4], [5]. Type II bursts result from spasmodic releases of GPE, generally attributed to instabilities in the accretion disk. They occur in rapid sequences, with burst durations ranging from ~ 2 s to ~ 680 s and recurrence intervals from ~ 10 s to ~ 1 hr [6].

This dissertation focuses exclusively on Type I bursts since Type II bursts are fuelled by accretion instabilities and involve different underlying physics outside the scope of this work. Hereafter, Type I bursts will be referred to simply as “bursts,” and any reference to Type II bursts will be denoted as “Type II.”

X-ray bursts were independently discovered in 1975 by Grindlay et al.[7] and Belian et al.[8]. These bursts are typically represented as light curves, where X-ray counts are plotted against time. X-ray burst light curves typically reveal a characteristic shape: a sharp rise in counts over a few seconds followed by a tail that resembles a power-law decay over a longer time frame [8].

Recently, a light curve of SAX J1808.4–3658, a millisecond X-ray Pulsar, showed an intriguing feature, a noticeable pause in counts during the rise to the first peak [9]. This feature is noteworthy as not only has the initial rise historically been modelled to be fast and relatively smooth [10] but the very nature of thermonuclear explosions, a runaway reaction, makes the idea of a stalling puzzling. Reinforcing this counter-intuitive observation was the discovery of a similar pause in counts from the X-ray binary MAXI J1807+132 [11].

The aim of this research is twofold, firstly to investigate modelling techniques for the rise phase of X-ray bursts; and secondly, to identify and analyse pauses within a provided list of candidate bursts [12].

This dissertation investigates modelling techniques by applying three-segment piecewise fits to selected bursts. While each segment is free to model any part of the light curve, it is anticipated that the first segment will depict the initial rise, the second may capture any potential pause, and the third

will represent the continued rise of the burst to its peak. Three distinct combinations of straight lines (S) and power laws (P) are tested. Additionally, the fits are repeated with the gradient of the second segment constrained to zero (i.e., flat), to assess whether this variation, which can aid in identifying potential pauses, is a valid method.

For clarity, any fitting in which the second segment is forced to be flat is referred to as “constrained”, while the completely free fitting is referred to as “unconstrained”.

Pauses will be identified using validated constrained three-segment fits. If a pause is detected and the fit passes a quality control (Filter 5), its parameters will guide the unconstrained fit, which requires initial values. To minimize confirmation bias, only the unconstrained fit results will be analysed for statistically significant pauses and subjected to quality checks.

The research presented in this dissertation primarily aims to investigate a relatively new phenomenon: the ‘pause’ observed in some LMXB X-ray burst light curves. Studying this feature is important as it may deepen our understanding of the physics behind thermonuclear X-ray bursts and shed light on LMXB dynamics and the accretion process. In addition, by exploring different modelling techniques, this work may offer guidance for future studies on modelling complex light curves.

The outline for the rest of the report is as follows: Core Theoretical Concepts and Background Information, Methods Taken in Data Processing, Results of Model Comparisons and Pause Identification, Discussion of Methods and Results, Implications for Future Research, and Conclusions.

2 Theoretical Background

2.1 Binary accretion physics

Roche lobe overflow

As discussed in the introduction, accretion in LMXBs mainly occurs via Roche lobe overflow. A detailed understanding of the foundations of this process is key to providing context for binary accretion physics.

The Roche lobe defines a gravitational boundary around a star in a binary system, within which material remains bound to that star. Donor stars are typically evolved off the main sequence, as supported by orbital period calculations ([13], [14], [15]). Having expanded during the later stages of stellar evolution, these stars can fill and exceed their Roche lobe. Once material overflows this boundary, it is no longer gravitationally bound to the donor and instead falls towards the compact object (NS or BH), through either, the inner Lagrangian point, or the compact object captures mass from the wind of the donor star [16].

Accretion disk formation and physics

Accretion disks are fundamental structures in many astrophysical systems. Since their observational discovery in 1962 by Giacconi et al. [17] they have provided insight into a range of high-energy interactions and extreme gravitational environments, including strong indirect evidence for black holes [18].

In the context of LMXBs, transferred material carries the orbital angular momentum of the binary system due to angular momentum conservation laws [19]. This angular momentum prevents direct infall of material onto the compact object. Instead, it forms a rotating structure – an accretion disk – where material moves in near Keplerian orbits around the NS or BH [10].

For accretion to proceed, angular momentum must be transported outwards through the disk, allowing inner material to fall in and, in the case of NSs, accumulate on the surface. This transport is facilitated by magnetohydrodynamic (MHD) turbulence [20], driven by the magneto-rotational instability (MRI) [21]. The MRI arises in weakly magnetised, differentially rotating flows. It amplifies small seed magnetic fields generating turbulence that acts as an effective viscosity, functionally equivalent to internal friction [16]. This turbulence transports angular momentum outwards allowing mass to travel inwards and GPE to be released as thermal and radiative energy.

GPE release and X-ray emissions in the accretion disk

The idea that viscosity plays a central role in converting GPE to radiation has long been established. As outlined in a 1981 review on accretion disks [22], viscosity within a gas disk leads to energy loss in the gas. Since the only available energy source is GPE, this energy loss causes the gas to move deeper into the gravitational potential well. Consequently, viscosity efficiently converts GPE into radiation.

Viscosity in the disk, provided by MRI-driven MHD turbulence, acts as an effective frictional force that converts GPE into heat as material spirals closer to the compact object. The resulting X-ray emission is twofold. First, the inner regions of the accretion disk produce thermal blackbody-like emission ([23],[24]), with temperatures recorded to reach 10^7 K [25]. Secondly, some photons are comptonized by an extended accretion disk corona with a typical radius of $\sim 50\ 000$ km [26], boosting them to higher X-ray energies.

The observed emission from the accretion disk can thus be well modelled as a combination of blackbody-like thermal emission and comptonized emission from an extended corona [26].

2.2 Physics of Neutron Stars and X-ray Bursts

Neutron star structure

At the end of a star's life, its fate is primarily determined by its mass. The resulting compact remnant can be one of three possibilities: a white dwarf (WD), a neutron star (NS), or a black hole (BH). The exact boundaries between initial masses of the progenitor forming WDs, NSs, or BHs are fairly uncertain, however typical mass ranges are well established and summarised in Table 1.

A key factor in this determination of compact remnant is the “Chandrasekhar limit” [28], defining a maximum mass a WD can have, approximately $1.4\ M_{\odot}$. Above this limit, electron degeneracy pressure supporting the WD is insufficient to counteract gravitational collapse, leading to formation of either a NS or BH [29].

Initial (M_{\odot})	Remnant Type	Typical Remnant Mass (M_{\odot})
$0.95 < M < 8 - 12$	WD (White Dwarf)	0.6
$8 - 11 < M < 25 - 30$	NS (Neutron Star)	1.35
$20 < M < 150$	BH (Black Hole)	~ 10

Table 1: Remnant Types and Typical Remnant Masses for Different Initial Mass Ranges [27]

WDs do not typically form LMXBs as they do not possess the necessary conditions for significant accretion. While BHs do form LMXBs, they lack a solid surface and instead feature an event horizon. In the context of this dissertation, which focuses on thermonuclear flashes (bursts) originating exclusively from the surface of neutron stars, only NSs will be discussed further.

NS structure can be summarised into five key components [29]:

Atmosphere – A very thin outer layer, only a few centimetres thick, primarily composed of hydrogen with possible heavier elements like helium and carbon.

Envelope – Approximately 100 m thick; acts as a thermal blanket between the hot interior ($T \sim 10^8$ K) and the ‘cold’ surface ($T \sim 10^6$ K) [30].

Crust – Approximately a 1 km thick, non-uniform region where, in the upper crust, electrons have been pressure ionized and move freely as a free Fermi gas.

Core – Composed of a uniform liquid mixture of neutrons, protons, electrons, and muons; accounting for $\sim 90\%$ of the NS mass and volume.

Exotic inner core (hypothetical) – Theorised to exist is an inner core containing exotic particles, such as hyperons, meson condensates, and quark matter [31]. It is important to note that, currently, no observational evidence confirms their existence.

Thermonuclear bursts (type – I)

Thermonuclear bursts manifest as a sudden increase in the X-ray intensity from a NS’s surface, typically exhibiting a blackbody-like spectrum of colour temperature $T_{bb} = 2\text{-}3$ keV (see Figure 1 for illustrative spectra shapes at these temperatures). As accreted material accumulates on the surface of the star it is compressed and heated hydrostatically, if the temperature is sufficiently high, hydrogen burns steadily into helium through the “hot” carbon-nitrogen-oxygen (CNO) process. Once thermonuclear ignition conditions are met, typically dominated by temperature and density, fuel at the base layer ignites and unstable burning spreads throughout, and consumes, all available fuel in a matter of seconds [5].

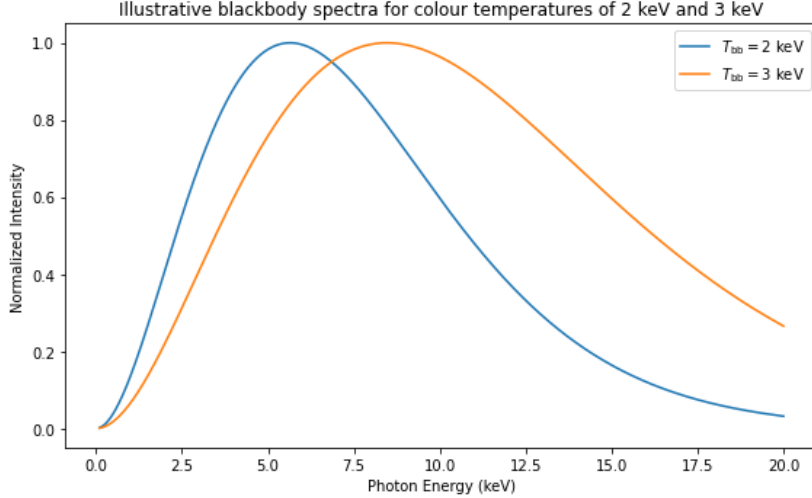


Figure 1: blackbody-like spectrum of colour temperature $T_{\text{bb}} = 2\text{-}3 \text{ keV}$, used to show outline of profile of typical thermonuclear bursts

Numerous numerical models of thermonuclear bursts have successfully reproduced key observables such as: rise times (seconds, $\sim 1 \text{ s}$ to 10 s), durations (minuets, tens to hundreds of seconds), recurrence times (hours), and total energies (10^{39} ergs to 10^{40} ergs) ([32]; [33]; [34]; [35]; [36]; [37]). The accuracy of these models has provided significant insight into the physical factors that shape these characteristics, including the composition of accreted fuel, metallicity, the amount of hydrogen burnt between bursts via the CNO cycle, the residual fuel remaining after a burst, and accretion rates.

Before delving into the accretion rate effects, it is necessary to introduce two key concepts: the Eddington luminosity (L_{Edd}) and local Eddington rate (\dot{m}_{Edd}).

L_{Edd} sets a fundamental limit on the maximum possible emission during a burst as it represents the point where radiation pressure outwards balances the inward gravitational pull. The Eddington limit also underpins the phenomenon of Photospheric Radius Expansion (PRE), whereby highly energetic bursts reach, or slightly exceed, the L_{Edd} . Beyond this point, the NS's photosphere begins to expand, with excess burst flux converted into kinetic and potential energy [38].

The Eddington luminosity L_{Edd} is given by the following expression:

$$L_{\text{Edd}} = \frac{4\pi GMm_p c}{\sigma_T} \quad (1)$$

Where: - G is the gravitational constant. - M is the mass of the stellar remnant. - m_p is the proton mass. - c is the speed of light. - σ_T is the Thomson scattering cross-section.

The local Eddington rate \dot{m}_{Edd} , is the maximum rate at which mass can be accreted onto a neutron star such that radiation produced by accretion does not exceed the Eddington luminosity, effectively, the point at which radiation pressure would blow away material. The local Eddington rate \dot{m}_{Edd} , is calculated from the total Eddington Rate \dot{M}_{Edd} , which is given by the following equation:

$$\dot{M}_{\text{Edd}} = \frac{L_{\text{Edd}}}{\eta c^2} \quad (2)$$

Where: - L_{Edd} is the Eddington luminosity. - η is the efficiency factor of the accretion process. - c is the speed of light.

The local Eddington rate \dot{m}_{Edd} is then calculated through dividing the total rate by surface area of the NS:

$$\dot{m}_{\text{Edd}} = \frac{\dot{M}_{\text{Edd}}}{4\pi R^2}$$

A calculation of L_{Edd} , and \dot{m}_{Edd} is performed for a typical NS with mass of $1.4M_{\odot}$, and radius of 10 km, and then compared to accepted values from literature in Appendix A to show how well these equations hold.

Now, Common thermonuclear ignition models for hydrogen (H) and helium (He) predict how bursts vary as a function of accretion rate ([39], [35], [40]). From these models, and building on various papers, Galloway et al. [5] proposed that regimes of thermonuclear ignition may be identified based on the local accretion rate presented as a fraction of the local Eddington rate:

Case 3 – low accretion rates, $\dot{m} \leq 0.01 \dot{m}_{\text{Edd}}$: H ignites unstably due to low temperatures, triggering He burning, leading to bursts in a H-rich environment [36].

Case 2 – Intermediate accretion rates, $0.01 \leq \dot{m}_{\text{Edd}} \leq 0.1$: H burns stably, leading to a growing He layer at the base of the accreted material, He ignites via the triple-alpha process, resulting in unstable, rapid, and intense He fuelled burst ([41], [37]).

Case 1 – High accretion rates, $0.1 \leq \dot{m}_{\text{Edd}} \leq 1$: H is accreted faster than it is burnt to He, resulting in unstable He ignition in a H-rich environment ([41], [42], [43]).

Case 0 – Very high accretions rates, $\dot{m} \approx \dot{m}_{\text{Edd}}$: Temperatures are high enough to facilitate stable He burning between bursts, depleting fuel reserves and causing bursts to cease altogether [39].

It is worth noting that there are other factors that could significantly change accretion rate at which bursting regimes occur and there are observation discrepancies that contradict the statements made above, however that falls outside the scope of this dissertation so will not be discussed further.

While the main aim of this dissertation, to investigate the pause phenomenon, may not be directly correlated to classification of burst types, understanding the theoretical background of these bursts is crucial. For example, early theories on the pause phenomenon postulated that such features could be linked to fuel composition or method of ignition [44]. This highlights the importance of theoretical models In proving context for observed burst behaviour.

Light curves

Light curves are time series plots that track the photon count rate of an astrophysical source as a function of time, and are commonly used, particularly in the study of X-ray bursts, to plot count rate against time. They serve as a fundamental diagnostic tool, enabling analysis of burst morphology, rise and decay profiles, and the identification of unusual phenomena.

In this dissertation, light curves are utilised to examine burst structure, with particular emphasis on the rise phase of bursts and the detection of pauses

Pause phenomenon

The first recorded acknowledgment of a pause was in 2019, Peter Bult et al. [9] reported on a bright, helium-fuelled, type I Xray bursts from the X-ray pulsar SAX J1808.4-36 (hereafter SAX J1808). With a bolometric flux of $(2.3 \pm 0.1) \times 10^{-7}$ ergs $^{-1}$ cm $^{-2}$, it is considered the brightest X-ray burst observed with the Neutron Star Interior Composition Explorer (NICER) mission to date.

Although only mentioned briefly, the authors noted a “noticeable pause during the rise to the first peak” a feature that went on to be the primary motivation behind this dissertation.

This pause lasted for ~ 0.7 seconds and occurred at $t \sim 0.6$ s (start of the burst is taken as $t = 0$). The count rate during the pause remained constant at $\sim 13,600$ ct s $^{-1}$ before continuing towards the maximum $\sim 34,000$ ct s $^{-1}$ at $t \sim 4.3$ s. The peak held for ~ 3.6 seconds before decaying to background levels at $t \sim 64$ s.

This burst from SAX J1808 also showed a double-peak structure in its light curve, with the first peak at $t \approx 4.3$ s (count rate $\approx 34,000$ ct s $^{-1}$) and the second peak at $t \approx 15.5$ s (count rate $\approx 16,500$ ct s $^{-1}$). This feature showed that both a pause and a double peak can exist simultaneously.

The second recorded acknowledgement of a pause came in 2020 from Albayati et al. [11]. This paper discussed three X-ray bursts from the H/He fuelled LMXB, MAXI J1807 +132 (hereafter MAXI J1807). The first burst (B1) showed a clear pause, the second burst (B2) showed no pause, and the third burst (B3) showed a possible pause. In the context of this paper, we will not accept the possibility of a pause during B3.

The pause in B1, occurred at $t \approx 2$ seconds and lasted for ≈ 1.6 s at a count rate of ≈ 500 ct s $^{-1}$. The burst then reached a peak at $t \approx 3.8$ s with a count rate of ≈ 2250 ct s $^{-1}$. A summary of the key characteristics of these bursts is presented in Table 2

Attribute	SAX J1808	MAXI J1807
Fuel type	He	H/He
Magnetic behaviour	Pulsar	Non-pulsar
Pause length	~ 0.7 s	~ 1.6 s
Peak count rate	$\sim 34,000$ ct s $^{-1}$	$\sim 2,250$ ct s $^{-1}$
Pause location as % of peak counts	$\sim 40\%$	$\sim 20\%$

Table 2: Comparison of attributes between SAX J1808 and MAXI J1807.

3 Methods

3.1 Data Collection & Initial Filtering

Process

Firstly, the quality of the bursts was assessed. 248 potential bursts from 50 sources were obtained from a database provided by Diego Altamirano [12] with 1 rapid burster being excluded, and 15 additional sources being excluded due to absence of detected bursts.

This initial processing, including the use of HEASoft software enabled raw data quality to be assessed, bursts to be identified, and data sample cleaning for further development.

Of the 124 potential bursts, 81 were successfully identified (Filter 1). Following quality assessment (Filter 2), 65 were retained for further development, while 16 were excluded based on failure criteria detailed in Table 3.

Relevant Methodology

Data used in this project was obtained from the Neutron Star Interior Composition Explorer (NICER) mission [45]. Launched in June of 2017, NICER is an X-ray telescope currently mounted on the International Space Station. With high throughput in the 0.2–12 keV energy range, combined with superb time resolution, NICER is an ideal instrument to search for discrete spectral features [46]. Data was obtained from NASA’s HEARSARC Browser [47].

Throughout this project, bursts were systematically excluded based on pre-determined quality control criteria and, later upon pause-specific constraints. These measures were taken to ensure that only bursts with sufficient and reliable data, were analysed. Multiple rounds of exclusion were applied at key stages, reflecting the evolving requirements of analysis. Exclusion criteria are summarised in Table 3.

N.	Justification for Exclusion	Filter 1 - rejections	Filter 2 - rejections
1	Absence of a distinct burst signature	12	2
2	Data dominated by noise or severe background contamination	4	11
3	Multiple expected bursts per source; fewer successfully recovered	6	0
4	Energy filtering constraints suppressing the burst rise phase	2	0
5	Burst amplitude insufficient for robust detection	6	3
6	Invalid or inaccessible OBSID; event files could not be retrieved	2	0
7	Light curve generation failure due to missing event bins ('no bins' error)	11	0

Table 3: Exclusion reasons, 'Filter 1 - rejections' shows for what reasons bursts were rejected in application of Filter 1, analogous for 'Filter 2 - rejections' - Acts as a tally table

Computational Tools and Data Processing

NICER data were processed using HEASoft, a unified package for X-ray data analysis [48]. Within HEASoft, we employed Xselect, a command-line interface to Ftools [49], to filter bursts and generate light curves, which were then saved for further analysis. Key commands and their explanations can be found in Appendix B

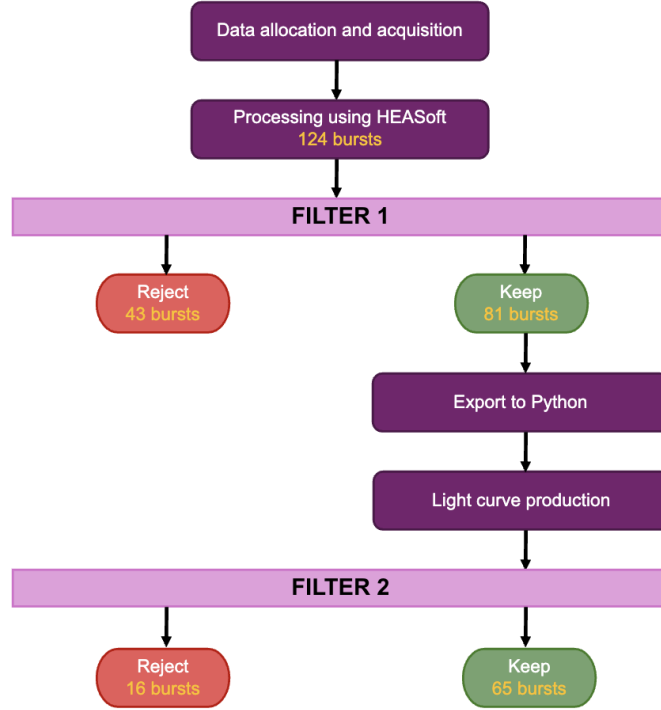


Figure 2: Flow diagram of the burst handling process described in Section 1.

3.2 Rise & Broad Plotting

Process

Following the initial processing, 65 bursts remained. Two plots were produced for each burst as in Figures 3 and 4, done to allow assessment of the rise phase without loosing the overall structure

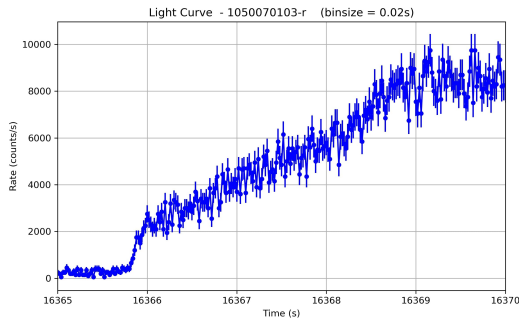


Figure 3: example rise plot

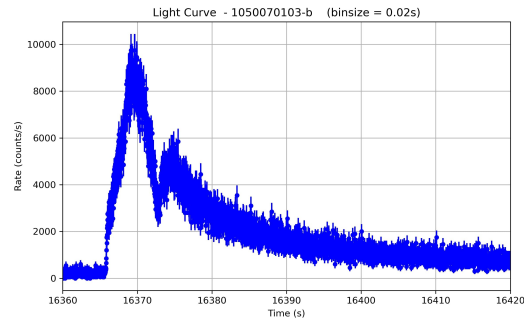


Figure 4: example broad plot

Rise and broad plots were generated for 53 of the 65 bursts; the remaining 12 were excluded due to large rise phase errors, even with increased time binning. Of the 53 bursts that were successfully plotted, 16 were rejected due to data being dominated by noise or severe background contamination, and another 8 were rejected due to an insufficient signal-to-noise ratio (Filter 3).

Potential pauses were identified in 26 of the remaining 29 bursts. This was determined by varying bin size from 0.01 s to 0.15 s and removing error bars to better visualise the data.

Relevant Methodology

Time binning posed a challenge: large bins could obscure features, while small bins led to high errors. Manual selection also risked confirmation bias. To mitigate this, a minimum pause length of 0.25 s was established based on a 95% confidence interval from known pauses (0.7 s and 1.6 s). Dividing this by three ensured at least three data points per pause, guiding binning choices. A refined binning method is detailed in the following section.

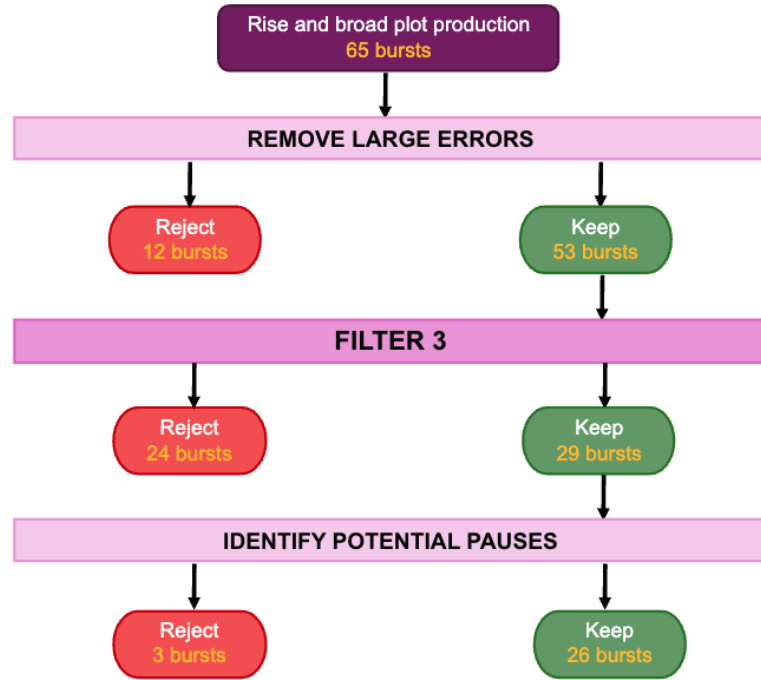


Figure 5: Flow diagram of the burst handling process described in Section 2.

3.3 Modelling Approaches

Process

The rise phase was modelled using three-segment piecewise fitting techniques. Each burst was first standardized to a time binning of 0.01s, then fitted with three segments intended to capture an initial rise, a potential pause, and a continued rise to the peak of the burst. Segments were either fitted straight lines (S) or power laws (P), and three distinct combinations were tested: S-S-S, P-S-S, and S-S-P. In addition, the fits were repeated with the gradient of the pause segment constrained to zero (i.e., flat), to investigate the potential of this adapted model for future pause detection.

All 26 bursts were fitted in the same manner, three unconstrained and three constrained fits were performed for each burst, resulting in a total of 156 fits. As the primary aim of this section was to investigate fitting models, the following step was taken to ensure fair comparison between constrained and unconstrained fits. Only the initial position parameters, not the gradient or power law parameters, were adjusted between the unconstrained and constrained fits.

During analysis, each fit was evaluated based on three criteria (Filter 4): (1) does the fit visually represent the data, i.e., does it pass through most of the data points? (2) is the reduced chi-squared value of the fit less than 2? and (3) is there a pause? The pause criteria were filled subjectively and doesn't contribute to rejection.

Relevant Methodology

Time binning was standardised to 0.01 s for all bursts processed in this section. This ensured consistency across the dataset and helped mitigate confirmation bias. Additionally, bursts that exhibited signs of pauses were later evaluated at different binning's to assess the robustness of the identified features.

The reduced chi-squared (χ^2_ν) is a statistical measure used to assess the goodness of fit between a model and observed data. Its use is employed across multiple different stages of data processing. It is calculated as the chi-squared statistic (χ^2) divided by the degrees of freedom (ν):

$$\chi^2_\nu = \frac{\chi^2}{\nu} \quad (3)$$

A reduced chi-squared value close to 1 indicates a good fit, suggesting the model accurately describes the data within the given uncertainties. For the context of noisy astrological data, a reduced chi-squared value of < 2 is considered acceptable.

Computational Tools and Data Processing

A Python script was provided by Giulio Mancuso [12], a Visiting PhD Student at the University of Southampton. It is designed to facilitate piecewise fitting of the burst data. The script initially included the first two fitting methods, S-S-S and P-S-S, and served as a robust foundation for further development of fitting methodology. It handled data import, defined a linear piecewise function, defined initial parameter guesses, performed curve fitting, and generated outputs including fitting parameters, errors, chi-squared values, and plots. A third fitting method (S-S-P) was added to expand

model comparisons and flat gradient variants were added for all three fitting combinations (constrained fitting).

`Piecewise_linear()`

Defines a piecewise function with four segments. The first segment is a constant value, representing background levels. The subsequent segments vary depending on the chosen fitting combination (e.g., for P-S-S : a power law for the rise phase, followed by two straight lines). The segments are determined by pivot points: x_{00} (end of the first segment), x_0 (end of the second segment), and x_1 (end of the third segment). Additionally, parameters for the slope and power law are defined for each segment.

`scipy.optimize.curve_fit`

This is the function used to perform non-linear least squares fitting, from the SciPy library [50]. It estimates best fit parameters for a given model function, here piecewise linear, by minimising differences between observed data and model prediction. The function takes in initial guess for the parameters and refines them based on the available data, returning fitted parameters and their estimated uncertainties.

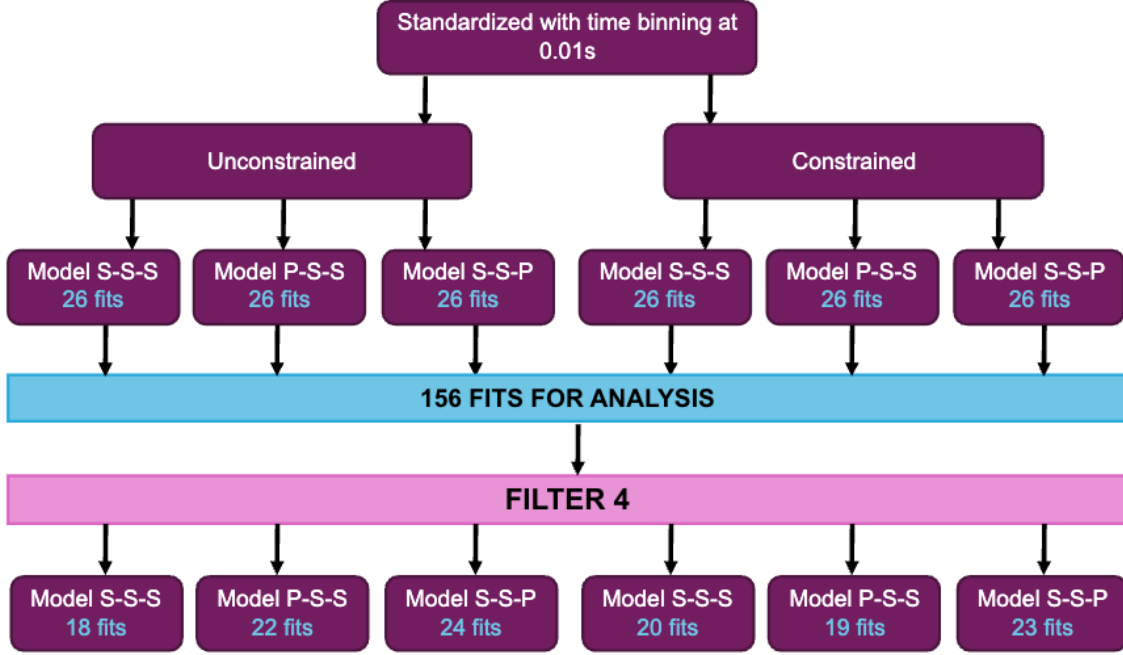


Figure 6: Flow diagram of the burst handling process described in Section 3.

3.4 Final Set of Fits

Process

Following the justification for the use of constrained models, detailed in Results section, constrained fitting models were applied to all 26 bursts using the three different fitting combinations. The purpose of this was to establish a systematic method for identifying potential pauses. Constrained fitting provided a way to roughly determine the presence and location of any such pauses in the rise phase of the burst, serving as a preliminary identification method prior to more detailed analysis.

In contrast to the approach described in Methods 3 where only position parameters were adjusted, all initial parameters were now allowed to vary. This was done to achieve the best possible fits within the constrained model framework. Following the fitting process, each burst was assessed against four quality control categories (Filter 5), as summarised in Table 4. Fits that failed two or more checks were rejected. After this selection process, 32 fits from 15 bursts were retained, out of a total of 78 fits attempted across 26 bursts.

The fitting parameters from the successful constrained fits were subsequently used to guide the initial parameter guesses for a corresponding mirrored fitting, this time using the unconstrained models. This was only performed for bursts that had passed the earlier quality control criteria. The purpose of this step was to mitigate bias introduced by the constrained models, which actively enforced flat regions and could artificially enhance the presence of pauses. Importantly, this approach also produced a final set of fits that could be used for the analysis of pause significance.

Relevant Methodology

Four quality control criteria were applied to the fits, intended to act as a filter for acceptable fits, though some level of subjectivity remained inherent. These criteria were: (1) does the fit visually represent the data, i.e., does it pass through most of the data points? (2) is the reduced chi-squared value of the fit less than 2? (3) does any identified ‘pause’ had a length greater than 0.25 s, based on the standard deviation calculations performed earlier; and (4) are individual parameter uncertainties smaller than 100% of their respective parameter values?

Number	Assessment Type	Pass N	Fail N
1	Visual inspection	62	16
2	χ^2	56	22
3	Pause length	8	70
4	Errors	48	30

Table 4: Assessment results for Filter 5, fits that failed ≥ 2 criteria are rejected

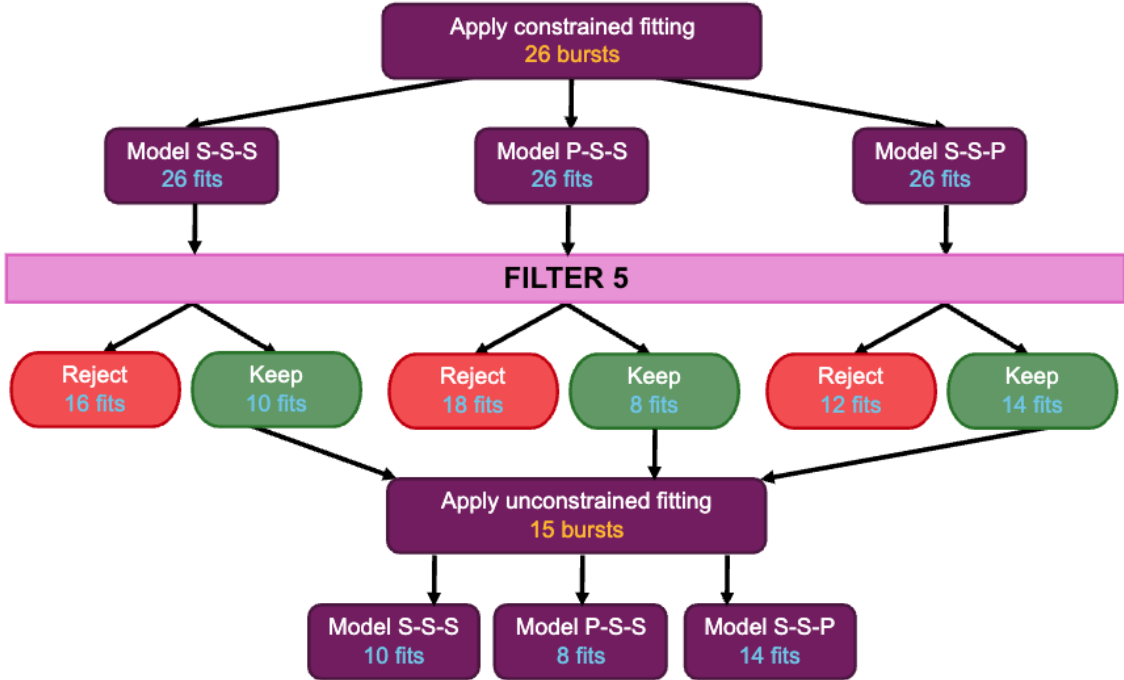


Figure 7: Flow diagram of the burst handling process described in Section 4.

3.5 Final Filtering

Process

This section began by establishing stricter criteria for pauses, with a pass/fail system implemented and detailed in the methodology section. It is important to note that while these criteria were more stringent than those used previously, they were not as strict as the final pause significance test, as the goal was to avoid prematurely excluding potential pauses.

Following the application of Filter 6, out of the 32 fits from 15 bursts that were tested, 14 fits from 10 bursts passed all constraints and thus qualified for robustness testing.

As detailed in earlier sections, time binning can significantly impact the detection of features such as pauses. To mitigate this, a standardized 0.01s time binning was applied prior to fitting. The 14 fits that passed all criteria were then repeated at time binning of 0.02 s and 0.05 s. This was done not only to test the robustness of the fitting parameters but also to allow for analysis comparing the fitting of the same burst at different binning resolutions. This marks the end of burst fitting, with the subsequent results and analysis to follow.

Relevant Methodology

To identify and evaluate pauses in the burst data, the following criteria were applied using a pass/fail system (Filter 6). These criteria were designed to ensure that robust and meaningful pauses were included for further analysis without being pre-emptively disqualifying pauses:

Pause Length: The pause length must exceed 0.5 times the combined error of the pause starts and end times.

Pause Slope: The slope during the pause must be less than 20% of the slopes from the segments before and after the pause region.

Overall Fit Quality: The overall quality of the fit must meet predefined standards, including acceptable residuals and chi-squared values.

Visual Inspection: The fit should visually match the data, ensuring it follows the trend of the observed points, while subjective a fail was only issue for extremely poor fits

Limitations of the methods used throughout this process are discussed in the Analysis.

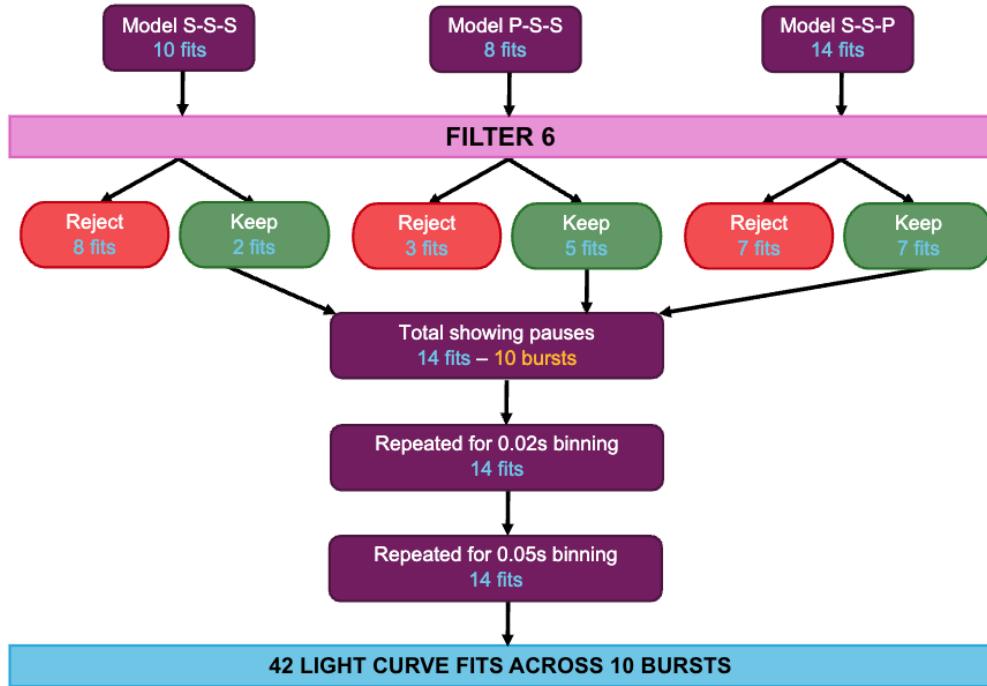


Figure 8: Flow diagram of the burst handling process described in Section 5.

3.6 Statistical Significance Testing

Process

42 Light curves were assessed for statistically significant pauses. In addition, the weighted mean and the appropriate error were calculated to allow further statistical assessment.

Relevant Methodology

In this study, a weighted mean was used in conjunction with different binning for assessment of pauses, The weighted mean is given by:

$$\bar{x} = \frac{\sum w_i x_i}{\sum w_i} \quad (4)$$

Where: x_i are the individual measurements, and w_i are the corresponding weights (typically the inverse of the variance or uncertainty).

The uncertainty associated with the weighted mean, $\sigma_{\bar{x}}$, is defined as:

$$\sigma_{\bar{x}} = \sqrt{\frac{1}{\sum w_i}} \quad (5)$$

Where: $w_i = \frac{1}{\sigma_i^2}$, and σ_i represents the uncertainty of each individual measurement x_i .

Statistical significance assessment is performed in two ways: through pause length and pause gradient significance tests.

To assess pause length significance, the pause length was divided by its associated error, yielding the significance in units of standard deviations (σ). A minimum threshold of 3σ was required for a pause to be considered significant.

To assess the significance of the pause gradient, the gradient value was divided by its associated error, giving the gradient's significance in terms of standard deviations (σ). A gradient was considered significant if the resulting value exceeded the 3σ threshold.

4 Results

4.1 Model Comparison

4.1.1 Constrained vs unconstrained, model comparison

A total of 156 fits at 0.01 s time binning (26 per model, across 6 modes) were available for analysis. Three sets of results were considered: the full set of fits (All-Fits), the subset remaining after the first filtering stage (A Filtered), and the subset after additional filtering (B Filtered).

For Filter A, fits failing both the first and second criteria found in Table 4 were excluded. For Filter B, if a constrained fit was removed, its unconstrained counterpart was also removed, and vice versa. The average reduced chi-square values (χ^2_ν) for each set, alongside errors, are presented in Table 5.

Variant	All-Fits		A Filtered		B Filtered	
	χ^2_ν	Uncertainty	χ^2_ν	Uncertainty	χ^2_ν	Uncertainty
Unconstrained	2.172	1.363	1.806	0.519	1.750	0.514
Constrained	2.315	2.927	1.778	0.403	1.756	0.414

Table 5: Summary of average reduced chi-squared (χ^2_ν) values and associated uncertainties for unconstrained and constrained fits across different filtering stages.

The number of fits used and the number removed at each filtering stage are summarized in Table 6.

Variant	All-Fits		A Filtered		B Filtered	
	Total Fits	Removed Fits	Total Fits	Removed Fits	Total Fits	Removed Fits
Unconstrained	78	0	64	14	53	25
Constrained	78	0	62	16	53	25

Table 6: Summary of total fits and number of removed fits for unconstrained and constrained cases across different filtering stages.

Key takeaways are as follows: filtering improves fit quality, with lower average (χ^2_ν) values for both approaches after First and Second filtering. The differences between the unconstrained and constrained fitting methods are reduced after filtering. The large uncertainties in the All-Fits set indicate greater variability in the total data set.

4.1.2 Piecewise model comparisons (S-S-S, P-S-S, and S-S-P)

This section presents the results of model testing for the three fitting models: S-S-S, P-S-S, S-S-P. The same three sets of results used in the previous section are considered, with the filtering remaining unchanged. Performance of models is based on their reduced chi-squared (χ^2_ν) values and associated uncertainties. The aim is to assess how well each model fits the data and how filtering impacted model performance. Results can be found in Table 7.

Variant	Model	All-Fits		A Filtered		B Filtered	
		χ^2	Uncertainty	χ^2	Uncertainty	χ^2	Uncertainty
Unconstrained	S-S-S	2.184	1.37	1.734	0.35	1.732	0.398
	P-S-S	2.256	1.608	1.788	0.406	1.691	0.394
	S-S-P	2.076	1.115	1.876	0.698	1.808	0.656
Constrained	S-S-S	2.063	0.684	1.83	0.323	1.852	0.362
	P-S-S	2.939	4.956	1.73	0.364	1.703	0.365
	S-S-P	1.943	0.859	1.773	0.503	1.737	0.482
Combined	S-S-S	2.124	1074	1.785	0.35	1.792	0.378
	P-S-S	2.598	3.664	1.761	0.379	1.697	0.374
	S-S-P	2.01	0.988	1.826	0.606	1.772	0.57

Table 7: Fit results showing χ^2 values and uncertainties for Models, S-S-S, P-S-S, and S-S-P across sets; All-Fits, A Filtered, and B Filtered.

S-S-S model: The best performing model in terms of both χ^2_ν and uncertainty, performing particularly well when filtering constrained data. This model is the most reliable model overall.

P-S-S model: The least reliable model as evidenced by its consistently higher χ^2_ν and uncertainty values, however this model shows the most significant improvement after applying filtering.

S-S-P model: This model offers a balanced performance compared to P-S-S, but it shows higher uncertainty than S-S-S. Also shows improvement in both χ^2_ν and uncertainty values after filtering.

Key takeaways are as follows: Filtering significantly improves all model fits, regardless of variant, by reducing the spread in uncertainty and bringing down the χ^2_ν values. Model S-S-S consistently appears to be the most robust, while model P-S-S shows higher χ^2_ν and uncertainty values particularly in the All-Fits Set.

4.2 Pause Significance

4.2.1 Statistical Testing

A total of 42 light curves across 10 bursts were analysed to identify statistically significant pauses, 19 significant pause lengths and 1 significant pause gradient were found. Each burst was assessed across three time binnings: 0.01 s, 0.02 s, and 0.05 s, as well as a weighted mean of parameters derived from these fittings. As described in Method 6, pauses are considered significant based on pause length and pause gradient criteria, 56 significance tests were performed. The results of this analysis are shown in Table 8 and summarised in Table 9.

OBSID	Model	bin 0.01 s		bin 0.02 s		bin 0.05 s		Average	
		Len (σ)	Grad (σ)	Len (σ)	Grad (σ)	Len (σ)	Grad (σ)	Len (σ)	Grad (σ)
1050010111	S-S-S	12.737	2.152	11.228	1.453	9.361	1.109	19.397	2.800
	P-S-S	11.588	4.838	11.188	1.862	9.310	1.400	18.797	5.113
	S-S-P	4.913	0.384	4.663	0.422	3.551	0.354	7.656	0.668
7050030105	P-S-S	2.145	0.265	2.157	0.305	1.989	0.243	3.635	0.470
1050070103	P-S-S	0.240	0.007	0.239	0.061	0.686	1.220	0.659	1.192
1050080112	S-S-P	3.595	0.279	3.775	0.301	6.951	0.569	8.833	0.488
1050080151	S-S-P	2.867	0.063	2.638	0.473	2.584	0.454	4.677	0.581
1050080173	S-S-P	2.849	0.001	3.120	0.101	3.237	0.753	5.443	0.526
1050080185	P-S-S	0.728	0.049	0.704	0.501	0.486	0.209	1.104	0.479
1050080190	S-S-S	0.943	0.085	1.050	0.211	0.948	0.017	1.705	0.196
	S-S-P	1.464	0.480	2.258	0.989	1.647	0.043	3.282	0.635
2050080209	P-S-S	0.944	0.295	1.289	0.193	1.154	0.172	1.932	0.349
	S-S-P	5.633	0.616	4.437	0.053	1.674	0.670	7.759	0.724
1050150127	S-S-P	7.418	0.008	6.723	0.933	26.717	0.706	37.199	0.976

Table 8: Length and gradient significance, in units of (σ), at three binning levels and a weighted average for each of the 14 fittings across 10 bursts. Significant findings are marked with red

Category	0.01s	0.02s	0.05s	Weighted Average	Total
Pause and Length Significant	1	0	1	1	3
Only Pause Significant	5	7	9	9	30
Only Gradient Significant	0	0	0	0	0
No Significance	8	7	4	4	23

Table 9: Table showing results from significance testing of 14 fits across 10 bursts. This table effectively acts as a tally system for each category.

A pause length or gradient is considered significant if it exceeds 3σ . Out of the 112 significance tests performed, 31 were found to be significant, corresponding to ten models across seven bursts. Of these 10 models, 5 showed significance in every pause length test, while the remaining 5 displayed ≥ 1 significant result. 4 fittings, across 4 bursts, showed no significant results.

Among the gradients, only three were calculated as significant, all corresponding to the P-S-S model of OBSID 1050010111. This model and burst demonstrated the highest consistency, with all tested models showing significant pause lengths across all binning and average methods.

4.2.1 Significant pause plots

Source: **4U_0513-40** OBSID: **1050010111** Model: **S-S-S**

Binning	Length	Length Error	Gradient	Gradient Error	Length (σ)	Gradient (σ)
0.01	9.930	0.780	13.004	6.044	12.737	2.152
0.02	9.536	0.849	10.410	7.164	11.228	1.453
0.05	9.551	1.020	9.690	8.741	9.361	1.109
Average	9.707	0.500	11.437	4.084	19.397	2.800

Table 10: Pause lengths are highly significant ($>9\ \sigma$) in all bins; gradients remain below $3\ \sigma$.

All four pause length tests for the S-S-S model applied to this burst exceed the $3\ \sigma$ threshold, confirming statistically significant pause lengths in every fitting. Pause-length significance ranges from $9.361\ \sigma$ at 0.05 s to $19.397\ \sigma$ in the weighted mean, demonstrating exceptional consistency across time bins. The gradient never exceeds $3\ \sigma$, instead ranging from $1.109\ \sigma$ at 0.05 s to $2.8\ \sigma$ in the weighted mean, reinforcing that pause length is the dominant significant feature in this burst. Relevant data is located in Table 10. **Taking the weighted average: Pause = $9.7\text{ s} \pm 0.5$**

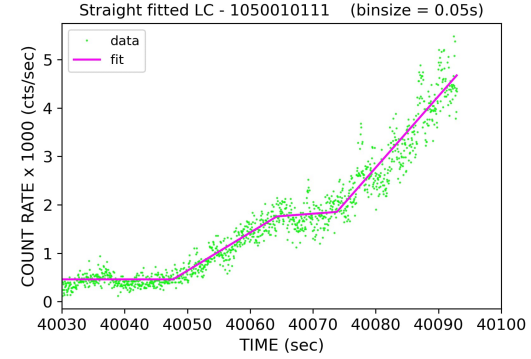
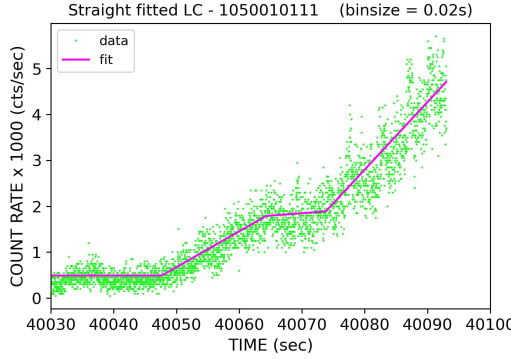
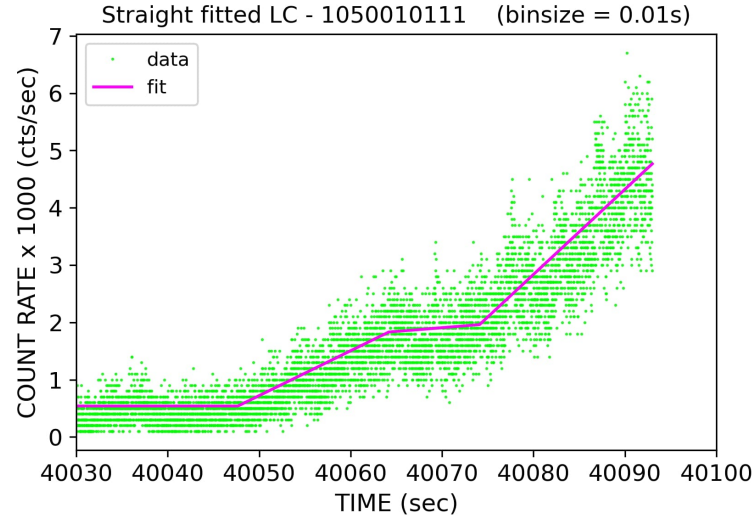


Figure 9: Fitted Light curves (1050010111). Top: 0.01 s bin; Bottom left: 0.02 s bin; Bottom right: 0.05 s bin.

Source: **4U_0513-40** OBSID: **1050010111** Model: **P-S-S**

Binning	Length	Length Error	Gradient	Gradient Error	Length (σ)	Gradient (σ)
0.01	11.423	0.986	23.529	4.863	11.588	4.838
0.02	10.118	0.904	12.309	6.610	11.188	1.862
0.05	10.091	1.084	11.400	8.142	9.310	1.400
Average	10.645	0.566	18.050	3.530	18.797	5.113

Table 11: Pause lengths are highly significant ($>9\ \sigma$) across all bins, with gradients exceeding $3\ \sigma$ at 0.01 s and for the weighted mean.

All four pause length tests for the P-S-S model applied to this burst exceeded the 3σ threshold, confirming statistically significant pause lengths in every fitting. Pause-length significances ranges from $9.310\ \sigma$ at 0.05 s to $18.797\ \sigma$ in the weighted mean, demonstrating strong consistency across time bins. The gradient reaches $4.838\ \sigma$ at 0.01 s and $5.113\ \sigma$ in the weighted mean, confirming one of the three fits has a significant gradient. Pause length remains the most significant feature across all bins. Relevant data is located in Table 11. **Taking the weighted average: Pasue = $10.6\text{ s} \pm 0.6$**

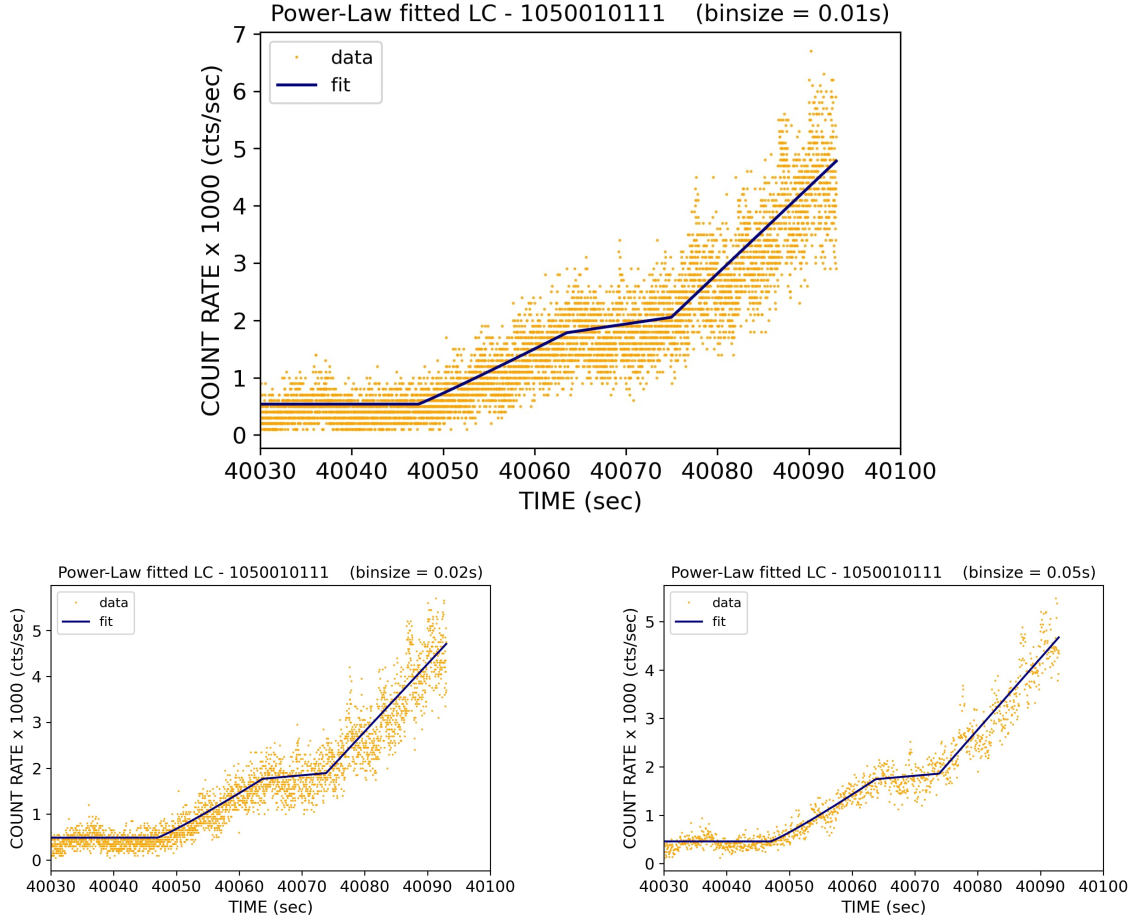


Figure 10: Fitted Light curves (1050010111). Top: 0.01 s bin; Bottom left: 0.02 s bin; Bottom right: 0.05 s bin.

Binning	Length	Length Error	Gradient	Gradient Error	Length (σ)	Gradient (σ)
0.01	5.467	1.113	-5.421	14.110	4.913	0.384
0.02	5.483	1.176	-6.603	15.641	4.663	0.422
0.05	5.264	1.483	-7.136	20.133	3.551	0.354
Average	5.431	0.709	-6.204	9.294	7.656	0.668

Table 12: Pause lengths are significant ($>3.5\sigma$) in all bins; gradients remain well below 3σ .

All four pause length tests for the S-S-P model applied to this burst exceed the 3σ threshold, confirming statistically significant pause lengths in every fitting. Pause-length significance ranges from 3.551σ at 0.05 s to 7.656σ in the weighted mean, demonstrating strong consistency across time bins. The gradient never exceeds 3σ , instead ranging from 0.384σ at 0.01 s to 0.668σ in the weighted mean, reinforcing that pause length is the dominant significant feature in this burst. Relevant data is located in Table 12. **Taking the weighted average: Pause = 5.4 s \pm 0.7**

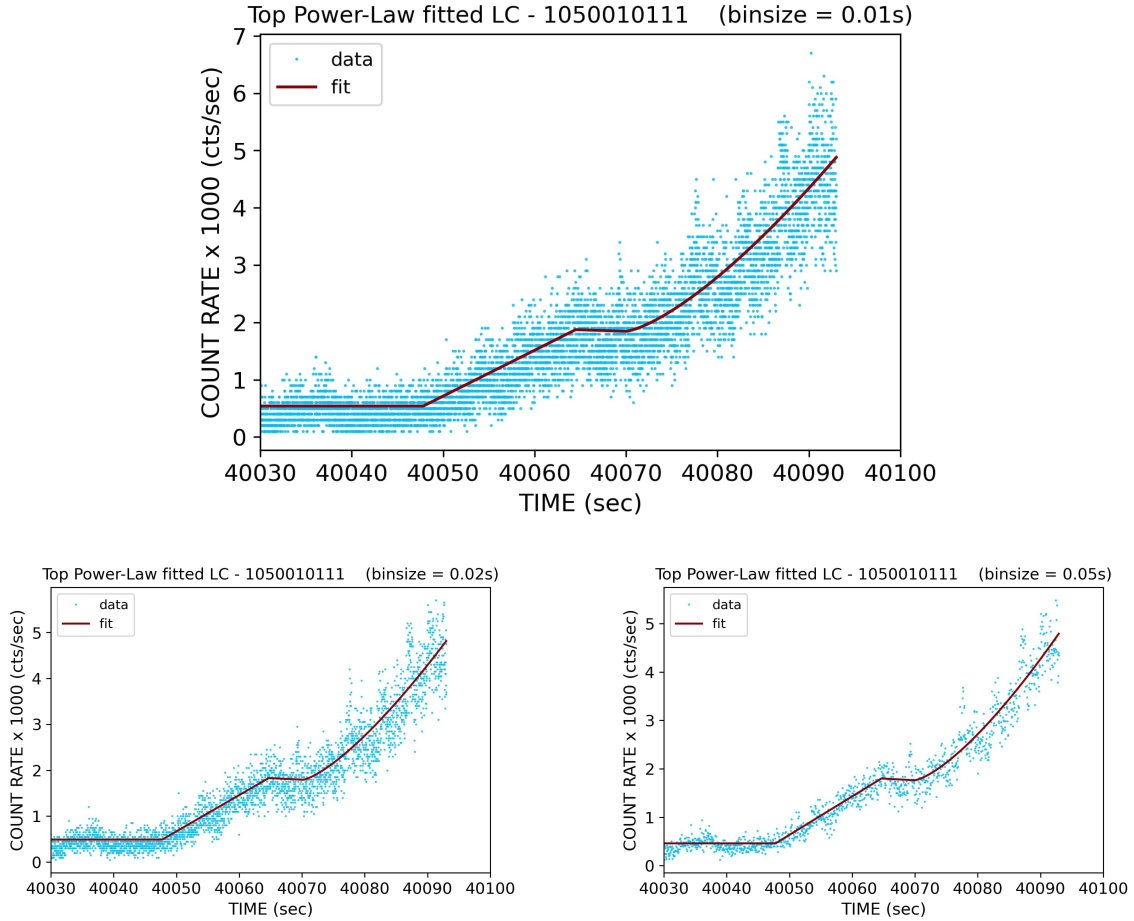


Figure 11: Fitted Light curves (1050010111). Top: 0.01 s bin; Bottom left: 0.02 s bin; Bottom right: 0.05 s bin.

Source: **4U_1636-536** OBSID: **1050080112** Model: **S-S-P**

Binning	Length	Length Error	Gradient	Gradient Error	Length (σ)	Gradient (σ)
0.01	0.404	0.112	164.917	590.541	3.595	0.279
0.02	0.353	0.094	-238.342	791.935	3.775	0.301
0.05	0.563	0.081	191.924	337.581	6.951	0.569
Average	0.471	0.053	134.245	274.857	8.833	0.488

Table 13: Pause lengths are significant ($>3.5\sigma$) in all bins; gradients remain well below 3σ .

All four pause length tests for the S-S-P model applied to this burst exceed the 3σ threshold, confirming statistically significant pause lengths in every fitting. Pause-length significance ranges from 3.595σ at 0.01 s to 8.833σ in the weighted mean, demonstrating strong consistency across time bins. The gradient never exceeds 3σ , instead ranging from 0.279σ at 0.01 s to 0.569σ at 0.05, reinforcing that pause length is the dominant significant feature in this burst. Relevant data is located in Table 13.

Taking the weighted average: Pause = $0.471\text{ s} \pm 0.053$

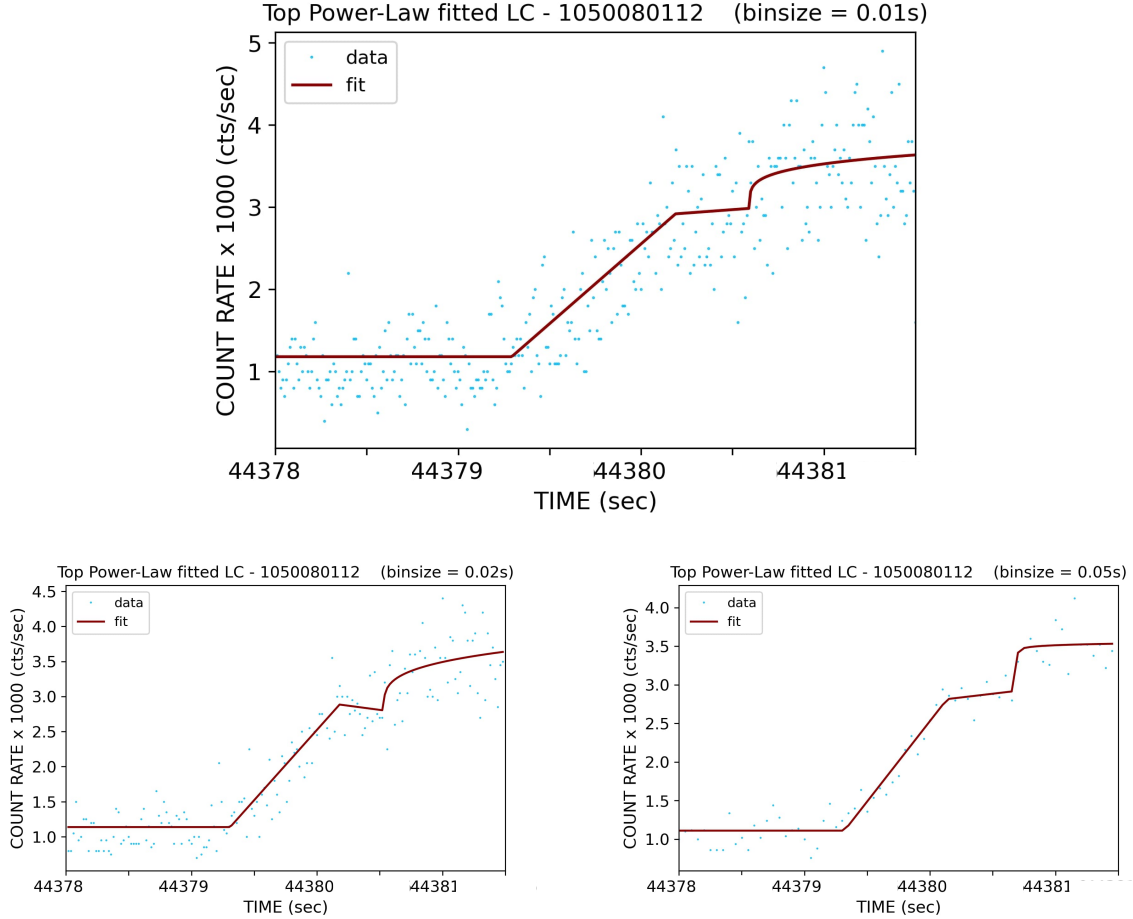


Figure 12: Fitted Light curves (1050080112). Top: 0.01 s bin; Bottom left: 0.02 s bin; Bottom right: 0.05 s bin.

Source: 4U_1728-34 OBSID: 1050150127 Model: S-S-P

Binning	Length	Length Error	Gradient	Gradient Error	Length (σ)	Gradient (σ)
0.01	0.511	0.069	-2.734	329.917	7.418	0.008
0.02	0.502	0.075	-298.161	319.638	6.723	0.933
0.05	0.535	0.020	-174.393	247.048	26.717	0.706
Average	0.530	0.014	-164.051	168.169	37.199	0.976

Table 14: Pause lengths are highly significant ($>6\ \sigma$) in all bins; gradients remain well below $3\ \sigma$.

All four pause length tests for the S-S-P model applied to this burst exceed the $3\ \sigma$ threshold, confirming statistically significant pause lengths in every fitting. Pause-length significance ranges from $6.723\ \sigma$ at 0.02 s to $37.199\ \sigma$ in the weighted mean, demonstrating extremely strong consistency across time bins. The gradient never exceeds $3\ \sigma$, instead ranging from $0.008\ \sigma$ at 0.01 s to $0.976\ \sigma$ in the weighted mean, reinforcing that pause length is the dominant significant feature in this burst. Relevant data is located in Table 14. **Taking the weighted average: Pause = $0.53\text{ s} \pm 0.014$**

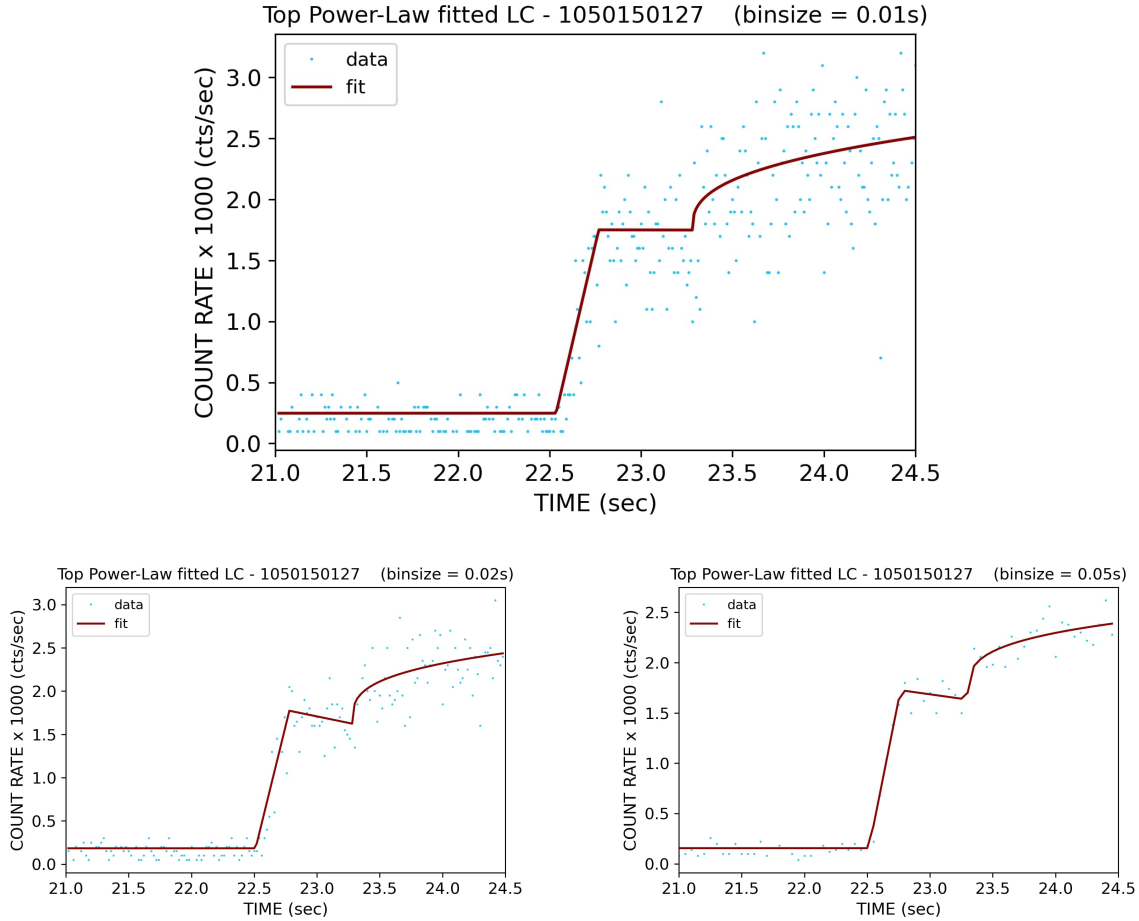


Figure 13: Fitted Light curves (1050150127). Top: 0.01 s bin; Bottom left: 0.02 s bin; Bottom right: 0.05 s bin.

5 Discussion

5.1 Interpretation of Model Analysis

Constrained Vs Unconstrained Model Comparison

Analysis of the constrained and unconstrained fitting methods reveals some interesting trends. Firstly, filtering of the data significantly improves the fit quality. This is an expected result, as one criterion that filtering was based upon was the individual χ^2_ν values that contributed to the totals; exclusion of high χ^2_ν values expectedly lowered the average χ^2_ν value.

Initially, unconstrained fitting performed better, another expected result, as the removal of a degree of freedom was an inherent part of the constrained fitting variant. It was anticipated that having fewer degrees of freedom would logically result in a slightly worse fit. The biggest result from this section was that after 'B Filtering' was applied, where equal numbers of fits are removed from both variants, the difference in performance between unconstrained and constrained fits shrunk. This indicates that, under appropriate filtering, differences between the two approaches become small enough to justify using the constrained, less free, variants of the models S-S-S, P-S-S, and S-S-P. Later this principle was utilized to allow use of the constrained model to search for pauses in a standardized manner.

Piecewise Model Comparisons (S-S-S, P-S-S, and S-S-P)

The first ultimate aim of this project was to investigate modelling techniques used for the rise phase of bursts, having been provided the means by which to fit rises, specifically the S-S-S and P-S-S piecewise models. A third model was introduced, S-S-P, which fits two straight lines followed by a power law. This was introduced during the early stages of fitting, as some bursts appeared to tail off towards the peak of the burst, and the two provided models were failing to achieve good fits.

The S-S-S model was the best performing model overall, achieving the lowest χ^2_ν values and uncertainties. However, this may be due to the simplistic nature of this model: simply fitting only straight lines means there is less error when it comes to guessing initial parameters, and one fewer initial parameter is needed compared to any model that incorporates a power law. Regardless, simplicity is not necessarily a negative, as overcomplicated models can introduce many more areas for error to occur.

The P-S-S model was the least reliable model, consistently achieving higher χ^2_ν values and uncertainties, especially in the All-Fits dataset. This may stem from the fact that the model is quite specific: for bursts that follow an initial power-law 'take off' shape, it worked well, as evidenced by the model showing the greatest improvement after filtering. Although, it is worth noting that the worst model will always have the most room to improve.

The S-S-P model showed balanced performance in the early fitting stages, providing key middle-ground coverage between the other models. Improving with filtering as expected, this model ultimately provided significant pause detection capabilities, finding the only two other significant pauses outside of the key finding for OBSID: 1050010111, with pause significance for all three models across all time binning. This model is the key finding of the research question posed regarding the investigation of modelling techniques for the rise phase of X-ray bursts.

5.2 Interpretation of Significant Pauses

Out of 42 fitted light curves, 19 significant pause lengths and 1 significant pause gradient were found. Three bursts showed significant pause lengths across all three binning resolutions tested: 0.01 s, 0.02 s, and 0.05 s. Additionally, a weighted average and associated error were calculated and found to be significant for all three.

4U_0513-40 OBSID: 1050010111

The burst from **4U_0513-40** is remarkable, showing significant pause lengths across all three binning methods and for all three models tested. This provides extremely strong evidence of a pause. While there is some discrepancy in the measured pause lengths, **9.7 s ± 0.5** in the S-S-S model, **10.6 s ± 0.6** in the P-S-S model, and **5.4 s ± 0.7** in the S-S-P model, the consistency of the pause location, combined with a statistically significant gradient in the P-S-S model at 0.01 s binning, provides strong evidence that a pause is occurring. Of the 9 fittings associated with this burst, only one showed a statistically significant pause gradient, P-P-S model at 0.01 binning, this is another indicator that this pause is real as achieving a significance of 3σ in gradient of flat segments is a challenge.

This variation in modelling was an interesting development and raised questions about the accuracy of the fit of a single model. Regardless of how many repetitions at different binnings support it. Upon closer inspection of the fitting data, shown in Appendix C, all three models fitted the start time as $t \approx 40064$ s. Both the S-S-S and P-S-S models fitted the end time as $t \approx 40074$ s, while the S-S-P model fitted the end time as $t \approx 40070$ s. in addition, S-S-P model fitting shows significantly larger errors on the gradient of the pause for all binning.

For these reasons, we reject the shorter pause time from the S-S-P model. This gives rise to the creation of a new weighted mean from the S-S-S and P-S-S models, resulting in a pause time of **pause = 10.07 s ± 0.38**. This pause is significantly longer than the two previous pauses found, which were approximately 0.7 s and 1.6 s, respectively. However, since the dataset of previous pauses consists of only two values, it would be unwise to judge solely based on that.

4U_1636-536 OBSID: 1050080112

The burst from **4U_1636-536** was identified using model S-S-P. The pause parameters are **pause = 0.471 s ± 0.053**. While this pause shows significance in pause length at all time binnings, the recent issue with the S-S-P model raises questions about the authenticity of this pause. While it is clear that 'something' is happening where the pause segment has been identified, it is not enough to present this burst as having a clear, significant pause. For those reasons it will be left out of the pause comparison next and discussed in Implications for Future Research.

4U_1728-34 OBSID: 1050150127

The burst from **4U_1728-34** was assessed to have pause parameters of **Pause = 0.53 s ± 0.014**, while showing statistical significance in pause length at all binnings, the statistical significance of the gradient of the pause was very low, $< 1\sigma$.

The pause was also identified using model S-S-P and the same concerns are prevalent here with this burst also being excluded from further comparisons. The fitting does however show an interesting

trend - a negative gradient for the pause section. While a negative gradient still needs to be statistically significant, it could be interpreted as evidence of a pause. In effect, a pause is a stalling of counts during the rise phase of a burst; a negative gradient suggests that X-ray counts fell during this period, consistent with a temporary halt of a bursts rise phase.

5.3 Pause comparison

With models S-S-S and P-S-S both agreeing on key pause parameters from the **4U_0513-40** burst, we can update the information regarding pauses initially detailed in Table 2, now presented in Table 15.

Attribute	SAX J1808	MAXI J1807	4U_0513-40
Fuel type	He	H/He	H/He
Magnetic behaviour	Pulsar	Non-pulsar	Non-pulsar
Pause length	~ 0.7 s	~ 1.6 s	~ 10 s
Peak count rate	$\sim 34,000$ ct s $^{-1}$	$\sim 2,250$ ct s $^{-1}$	$\sim 5,000$ ct s $^{-1}$
Pause location as % of peak counts	$\sim 40\%$	$\sim 20\%$	$\sim 40\%$

Table 15: Comparison between SAX J1808, MAZI J1807, and 4U_0513-40, pause criteria taken from this report, Fuel type and magnetic behaviour from Koliopanos et al.[51]

Table 15 provides a comparison between the two previously known pauses and the newly identified pause deemed statistically significant in this report. 4U_0513-40 stands out due to its significantly longer pause length and moderate count rate, compared to SAX J1808, a pulsar exhibiting much higher burst intensities. Table 15 highlights that, while there are some similarities, there is considerable variation in both the characteristics of the pauses and the properties of the host LMXB.

5.4 Limitations

A key limitation in this report is subjectivity. Early in the methodological process, candidate bursts were often rejected for subjective reasoning, such as large errors or no potential pause. This may have introduced bias into the sample towards only the most “attractive” candidates.

Small sample size is another concern. Strict quality-control filters reduced the final burst set to just a fraction of the original pool. Although intended to ensure reliable fits, this may have discarded bursts that did contain pauses but failed initial, subjective screening.

5.5 Implications for Future Research

The investigation of fitting methods offers valuable guidance for future studies, pauses aren’t the only noteworthy features in burst light curves, and improvements in modelling could yield unexpected benefits for LMXB research.

Although only one burst exhibited a consistently significant pause, several others showed a significant pause under one or two fittings. Those bursts shouldn’t be dismissed; with alternative fitting approaches, they might yet reveal clear pauses.

At minimum, this work demonstrates that pauses potentially occur in more than a handful of bursts. That finding lays the groundwork for a broader survey, where applying these techniques to a larger sample could identify and catalogue pauses across many LMXBs.

With the uncertainty surrounding the S-S-P model, a future path of invalidating or verifying the model is left open. Additionally, if it is found to be valid, then two more pauses automatically become valid once again and could be used for further analysis.

6 Conclusion

This report investigated modelling techniques for the rise phase of X-ray bursts from LMXBs, with the ultimate aim of investigating the pause phenomenon first identified in 2019 by Bult et al.[9].

Relevant theory, such as binary accretion physics and specifics of thermonuclear bursts are explored to provide relevance and understanding of the core physics principles underpinning X-ray bursts. Additionally, the discovery of the pause phenomenon from X-ray pulsar SAX J1808.4-36 and a subsequent discovery of a different pause from LMXB, MAXI J1807 are detailed.

Starting with 124 bursts, and subsequently filtering down to 26, analysis on fitting models and fitting model variant was performed on a total of 156 fits. Three different fitting models were trialled, each a distinct combination of straight lines (S), and power-laws (P). Model S-S-S, model P-S-S, and model S-S-P. Filtering criteria was also applied during sannyasi to allow investigation of performance under key constraints.

For each model there are two variants: a 'unconstrained' version, where all fitting parameters are allowed to vary to find the best fit, and a 'constrained' version, where the gradient of the second segment was forced to be flat. The constrained variation was created in the hopes of providing a systematic methods for identifying potential pauses in the rise phase of X-ray bursts.

Following the model testing, and filtering down to 10 bursts. Statistical significance tests were performed on identified 'pauses' across different time binning to assess robustness of the pause found.

Statistically significant pauses ($>3\sigma$) were found in three different bursts, one of these pauses, from 4U_0513-40, was extremely well defined and supported, having been successfully fitted for pauses using all three models (S-S-S, P-S-S, S-S-P). The pause found is defined as 10.07 ± 0.38 . The other two bursts showing statistically significant pauses are defined as 0.471 ± 0.053 and 0.53 ± 0.014 respectively. However, while still showing some significance, due to model concerns laid out in discussions, they are not considered as robust as the one found from 4U_0513-40.

To further this research, deeper understanding and improved modelling methods for the rise phase of X-ray bursts is crucial as without sufficiently successful models, extraction of features from the background noise can not only be a challenging task but almost impossible for small, delicate features.

A Calculating L_{Edd} and \dot{m}_{Edd}

For a typical NS with mass of $1.4M_{\odot}$ solar and radius of 10km we calculate the L_{Edd} , and the \dot{m}_{Edd} as follows:

$$L_{\text{Edd}} = \frac{4\pi GMm_p c}{\sigma_T}$$

$$L_{\text{Edd}} = \frac{4\pi(6.674 \times 10^{-11})(2.7846 \times 10^{30})(1.6726 \times 10^{-27})(3 \times 10^8)}{6.652 \times 10^{-29}}$$

$$L_{\text{Edd}} \approx 1.76 \times 10^{38} \text{ J/s}$$

$$L_{\text{Edd}} \approx 1.76 \times 10^{38} \text{ erg/s}$$

$$\dot{M}_{\text{Edd}} = \frac{\dot{L}_{\text{Edd}}}{\eta c^2}$$

$$\dot{M}_{\text{Edd}} = \frac{1.8 \times 10^{38} \text{ erg/s}}{0.2 \times (3 \times 10^{10} \text{ cm/s})^2}$$

$$\dot{M}_{\text{Edd}} \approx 1 \times 10^{18} \text{ g/s}$$

$$\dot{m}_{\text{Edd}} = \frac{\dot{M}_{\text{Edd}}}{4\pi R^2}$$

$$\dot{m}_{\text{Edd}} = \frac{1 \times 10^{18} \text{ g/s}}{1.26 \times 10^{13} \text{ cm}^2}$$

$$\dot{m}_{\text{Edd}} \approx 8 \times 10^4 \text{ g cm}^{-2} \text{ s}^{-1}$$

$$\dot{m}_{\text{Edd}} \approx 1.3 \times 10^{-8} M_{\odot} \text{ yr}^{-1}$$

The calculated Eddington Luminosity (L_{Edd}) of 1.76×10^{38} erg/s is in good agreement with measured values: $(3.0 \pm 0.6) \times 10^{38}$ erg/s by Lewin et al. [52], and more recently $(3.79 \pm 0.15) \times 10^{38}$ erg/s by Kuulkers et al. [53]. The calculated local Eddington rate (\dot{m}_{Edd}) of 8×10^4 g cm $^{-2}$ is also in good agreement with calculations in the literature - Galloway et al. [5] calculated it to be 8.8×10^4 g cm $^{-2}$ s $^{-1}$.

B Key commands and explanations

`Start_xray_asimov_6.29_full`

Initializes HEASoft environment, 6.29 refers to the version number of the HEASoft software suite.

`nicerL2 indir=OBSID clobber=YES`

Runs NICER level-2 calibration that includes standard calibration, screening and filtering of data [54],

clobber=YES overwrites existing files in the output directory.

xselect

Launches Xselect to allow reading in of events and application of key Ftools listed below.

```
set binsize 0.01
```

Sets the time bin size on the light curve, here 0.01s. Smaller bin sizes yield more accurate representations of true observed counts but introduce larger errors due to fewer counts per bin.

```
filter pha_cut 30 1000
```

Applies an energy filter with lower (30) and upper (1000) cutoff, here corresponding to 0.3–10 keV (note: pha = pulse height amplitude). This filter removes photons outside of this energy range, standard practise for NICER observations of compact objects as it ensures relevant data and reduces background noise.

C 1050010111, fitting data for S-S-S, P-S-S, and S-S-P

OBSID	Fitting Model	Binning (s)	x_0	x_0 err	x_1	x_1 err	m	m err
1050010111	S-S-S	0.01	40064.169	0.720	40074.099	0.299	13.004	6.044
		0.02	40064.262	0.780	40073.798	0.336	10.410	7.164
		0.05	40064.252	0.936	40073.803	0.406	9.690	8.741
		Average	40064.222	0.461	40073.928	0.196	11.437	4.084
1050010111	P-S-S	0.01	40063.519	0.939	40074.942	0.300	23.529	4.863
		0.02	40063.721	0.840	40073.839	0.335	12.309	6.610
		0.05	40063.752	1.005	40073.843	0.406	11.400	8.142
		Average	40063.665	0.531	40074.310	0.196	18.050	3.530
1050010111	S-S-P	0.01	40064.490	0.649	40069.957	0.904	-5.421	14.110
		0.02	40064.679	0.713	40070.162	0.935	-6.603	15.641
		0.05	40064.652	0.872	40069.916	1.199	-7.136	20.133
		Average	40064.593	0.420	40070.024	0.571	-6.204	9.294

Table 16: Table showing data associated with the fittings of 4U_0513-40, x_0 = start time of pause, x_1 = end time of pause, m = gradient of the pause. This data is used to justify how they all model the same start time, x_0 , then S-S-P model deviates from the other two with its end time x_1 , and shows significantly higher errors on gradient

References

- [1] GJ Savonije. Roche-lobe overflow in x-ray binaries. *Astronomy and Astrophysics*, vol. 62, no. 3, Jan. 1978, p. 317–338. Research supported by the Nederlandse Organisatie voor Zuivere Wetenschappelijk Onderzoek and Universiteit van Amsterdam., 62:317–338, 1978.
- [2] Shan-Shan Weng and Shuang-Nan Zhang. Comparing the accretion disk evolution of black hole and neutron star x-ray binaries from low to super-eddington luminosity. *The Astrophysical Journal*, 739(1):42, 2011.

- [3] Jeffrey A Hoffman, Herman L Marshall, and Walter HG Lewin. Dual character of the rapid burster and a classification of x-ray bursts. *Nature*, 271(5646):630–633, 1978.
- [4] Sudip Bhattacharyya and Tod E Strohmayer. A non-pre double-peaked burst from 4u 1636–536: Evidence of burning front propagation. *The Astrophysical Journal*, 636(2):L121, 2006.
- [5] Duncan K Galloway, Michael P Muno, Jacob M Hartman, Dimitrios Psaltis, and Deepto Chakrabarty. Thermonuclear (type i) x-ray bursts observed by the rossi x-ray timing explorer. *The Astrophysical Journal Supplement Series*, 179(2):360, 2008.
- [6] Walter HG Lewin, Robert E Rutledge, Jefferson M Kommers, Jan van Paradijs, and Chryssa Kouveliotou. A comparison between the rapid burster and gro j1744–28. *The Astrophysical Journal*, 462(1):L39, 1996.
- [7] J Grindlay and H Gursky. Scattering model for x-ray bursts-massive black holes in globular clusters. *Astrophysical Journal, vol. 205, May 1, 1976, pt. 2, p. L131-L133.*, 205:L131–L133, 1976.
- [8] RD Belian, JP Conner, and WD Evans. The discovery of x-ray bursts from a region in the constellation norma. *Astrophysical Journal, vol. 206, June 15, 1976, pt. 2, p. L135-L138. DOD-ERDA-sponsored research.*, 206:L135–L138, 1976.
- [9] Peter Bult, Gaurava K Jaisawal, Tolga Güver, Tod E Strohmayer, Diego Altamirano, Zaven Arzoumanian, David R Ballantyne, Deepto Chakrabarty, Jérôme Chenevez, Keith C Gendreau, et al. A nicer thermonuclear burst from the millisecond x-ray pulsar sax j1808. 4–3658. *The Astrophysical Journal Letters*, 885(1):L1, 2019.
- [10] Nicolai Ivanovich Shakura and Rashid Alievich Sunyaev. Black holes in binary systems. observational appearance. *Astronomy and Astrophysics, Vol. 24, p. 337-355*, 24:337–355, 1973.
- [11] AC Albayati, Diego Altamirano, Gaurava K Jaisawal, Peter Bult, S Rapisarda, Giulio Cesare Mancuso, T Güver, Zaven Arzoumanian, Deepto Chakrabarty, Jérôme Chenevez, et al. Discovery of thermonuclear type-i x-ray bursts from the x-ray binary maxi j1807+ 132. *Monthly Notices of the Royal Astronomical Society*, 501(1):261–268, 2021.
- [12] NICER Team. Private communication, 2025. Private communication.
- [13] Roger A Chevalier. Neutron star accretion in a supernova. *Astrophysical Journal, Part 1 (ISSN 0004-637X), vol. 346, Nov. 15, 1989, p. 847-859.*, 346:847–859, 1989.
- [14] Jeffrey E McClintock and Ronald A Remillard. The x-ray nova centaurus x-4-comparisons with a0620-00. *Astrophysical Journal, Part 1 (ISSN 0004-637X), vol. 350, Feb. 10, 1990, p. 386-394.*, 350:386–394, 1990.
- [15] Bt Paczynski and R Sienkiewicz. The minimum period and the gap in periods of cataclysmic binaries. *Astrophysical Journal, Part 1 (ISSN 0004-637X), vol. 268, May 15, 1983, p. 825-831.*, 268:825–831, 1983.
- [16] Dimitrios Psaltis. Accreting neutron stars and black holes: a decade of discoveries. *arXiv preprint astro-ph/0410536*, 2004.
- [17] Riccardo Giacconi, Herbert Gursky, Frank R Paolini, and Bruno B Rossi. Evidence for x rays from sources outside the solar system. *Physical Review Letters*, 9(11):439, 1962.

- [18] Jeffrey E McClintock and Ronald A Remillard. The black hole binary a0620-00. *Astrophysical Journal, Part 1 (ISSN 0004-637X)*, vol. 308, Sept. 1, 1986, p. 110-122., 308:110–122, 1986.
- [19] Renee M Ludlam. Reflecting on accretion in neutron star low-mass x-ray binaries. *Astrophysics and Space Science*, 369(1):16, 2024.
- [20] Steven A Balbus and John CB Papaloizou. On the dynamical foundations of α disks. *The Astrophysical Journal*, 521(2):650, 1999.
- [21] Steven A Balbus and John F Hawley. Instability, turbulence, and enhanced transport in accretion disks. *Reviews of modern physics*, 70(1):1, 1998.
- [22] James E Pringle. Accretion discs in astrophysics. In: *Annual review of astronomy and astrophysics. Volume 19. (A82-11551 02-90) Palo Alto, CA, Annual Reviews, Inc., 1981*, p. 137-162., 19:137–162, 1981.
- [23] Kazuhisa Mitsuda, Hajime Inoue, Norio Nakamura, and Yasuo Tanaka. Luminosity-related changes of the energy spectrum of x1608-522. *Astronomical Society of Japan, Publications (ISSN 0004-6264)*, vol. 41, no. 1, 1989, p. 97-111., 41:97–111, 1989.
- [24] Richard L White. Synchrotron emission from chaotic stellar winds. In *Radio Stars: Proceedings of a Workshop on Stellar Continuum Radio Astronomy Held in Boulder, Colorado, USA, 8–10 August 1984*, pages 45–46. Springer, 1985.
- [25] MJ Church, AN Parmar, M Balucinska-Church, T Oosterbroek, D Dal Fiume, and M Orlandini. Progressive covering in dipping and comptonization in the spectrum of xb1916-053 from the beppoax observation. *arXiv preprint astro-ph/9806223*, 1998.
- [26] MJ Church and M Bałucińska-Church. Results of a lmxb survey: Variation in the height of the neutron star blackbody emission region. *Astronomy & Astrophysics*, 369(3):915–924, 2001.
- [27] Konstantin A Postnov and Lev R Yungelson. The evolution of compact binary star systems. *Living Reviews in Relativity*, 17(1):3, 2014.
- [28] Subrahmanyam Chandrasekhar. The maximum mass of ideal white dwarfs. *Astrophysical Journal*, vol. 74, p. 81, 74:81, 1931.
- [29] Jorge Piekarewicz. Nuclear physics of neutron stars. In *AIP Conference Proceedings*, volume 1128, pages 144–153. American Institute of Physics, 2009.
- [30] Dany Page, James M Lattimer, Madappa Prakash, and Andrew W Steiner. Minimal cooling of neutron stars: A new paradigm. *The Astrophysical Journal Supplement Series*, 155(2):623, 2004.
- [31] Dany Page and Sanjay Reddy. Dense matter in compact stars: Theoretical developments and observational constraints. *Annu. Rev. Nucl. Part. Sci.*, 56(1):327–374, 2006.
- [32] Masayuki Y Fujimoto, Mirek Sztajno, Walter HG Lewin, and Jan Van Paradijs. On the theory of type i x-ray bursts-the energetics of bursts and the nuclear fuel reservoir in the envelope. *Astrophysical Journal, Part 1 (ISSN 0004-637X)*, vol. 319, Aug. 15, 1987, p. 902-915. Research supported by the John Simon Guggenheim Memorial Foundation and Max-Planck-Gesellschaft zur Foerderung der Wissenschaften., 319:902–915, 1987.

- [33] S Ayasli and PC Joss. Thermonuclear processes on accreting neutron stars-a systematic study. *Astrophysical Journal, Part 1*, vol. 256, May 15, 1982, p. 637-665., 256:637–665, 1982.
- [34] Ikko Fushiki and DQ Lamb. New insights from a global view of x-ray bursts. *Astrophysical Journal, Part 2-Letters to the Editor (ISSN 0004-637X)*, vol. 323, Dec. 1, 1987, p. L55-L60., 323:L55–L60, 1987.
- [35] Lars Bildsten. Gravitational radiation and rotation of accreting neutron stars. *The Astrophysical Journal*, 501(1):L89, 1998.
- [36] Andrew Cumming and Lars Bildsten. Rotational evolution during type i x-raybursts. *The Astrophysical Journal*, 544(1):453, 2000.
- [37] Stanley E Woosley, Alex Heger, Andrew Cumming, Robert D Hoffman, Jason Puet, Thomas Rauscher, Jacob L Fisker, Hendrik Schatz, BA Brown, and M Wiescher. Models for type i x-ray bursts with improved nuclear physics. *The Astrophysical Journal Supplement Series*, 151(1):75, 2004.
- [38] Tomoyuki Hanawa and Daiichiro Sugimoto. Helium shell flash on accreting neutron stars-effects of hydrogen-rich envelope and recurrence of x-ray bursts. *Publications of the Astronomical Society of Japan*, Vol. 34, P. 1, 1982, 34:1, 1982.
- [39] Masayuki Y Fujimoto, Tomoyuki Hanawa, and Shigeki Miyaji. Shell flashes on accreting neutron stars and x-ray bursts. *Astrophysical Journal, Part 1*, vol. 247, July 1, 1981, p. 267-278. Ministry of Education, Science, and Culture of Japan, 247:267–278, 1981.
- [40] Ramesh Narayan and Jeremy S Heyl. Thermonuclear stability of material accreting onto a neutron star. *The Astrophysical Journal*, 599(1):419, 2003.
- [41] Duncan K Galloway and Andrew Cumming. Helium-rich thermonuclear bursts and the distance to the accretion-powered millisecond pulsar sax j1808. 4–3658. *The Astrophysical Journal*, 652(1):559, 2006.
- [42] Tamara S Galloway, Rebecca J Brown, Mark A Browne, Awantha Dissanayake, David Lowe, Malcolm B Jones, and Michael H Depledge. A multibiomarker approach to environmental assessment. *Environmental Science & Technology*, 38(6):1723–1731, 2004.
- [43] Jacob Lund Fisker, Hendrik Schatz, and Friedrich-Karl Thielemann. Explosive hydrogen burning during type i x-ray bursts. *The Astrophysical Journal Supplement Series*, 174(1):261, 2008.
- [44] Simon Guichardut and Andrew Cumming. The imprint of convection on type i x-ray bursts: Pauses in photospheric radius expansion lightcurves. *The Astrophysical Journal*, 954(1):54, 2023.
- [45] Keith Gendreau and Zaven Arzoumanian. Searching for a pulse. *Nature Astronomy*, 1(12):895–895, 2017.
- [46] TE Strohmayer, D Altamirano, Z Arzoumanian, Peter M Bult, D Chakrabarty, J Chenevez, AC Fabian, KC Gendreau, S Guillot, GK Jaisawal, et al. Nicer discovers spectral lines during photospheric radius expansion bursts from 4u 1820- 30: Evidence for burst-driven winds. *The Astrophysical Journal Letters*, 878(2):L27, 2019.
- [47] HEASARC. HEASARC Browse: High Energy Astrophysics Science Archive Research Center. <https://heasarc.gsfc.nasa.gov/db-perl/W3Browse/w3browse.pl>, 2025. Accessed 2025.

- [48] HEASARC. HEASoft: Unified Release of FTOOLS and XANADU. <https://heasarc.gsfc.nasa.gov/docs/software/heasoft/>, 2014. NASA High Energy Astrophysics Science Archive Research Center (HEASARC).
- [49] J. Ingham, K. A. Arnaud, and M. F. Corcoran. *The Xselect User's Guide*. NASA/GSFC, 1992. Version 1.0.
- [50] Pauli Virtanen, Ralf Gommers, Travis E. Oliphant, Matt Haberland, Tyler Reddy, David Cournapeau, Evgeni Burovski, Pearu Peterson, Warren Weckesser, Jonathan Bright, Stéfan J. van der Walt, Matthew Brett, Joshua Wilson, K. Jarrod Millman, Nikolay Mayorov, Andrew R. J. Nelson, Eric Jones, Robert Kern, Eric Larson, C. J. Carey, Štěpán Roučka, Damian E. Jones, Nicholas T. Barnett, Antony J. Warmenhoven, Juan Luis Cano, Kyle Kelley, André de Ribaupierre, Sebastian H. Markel, Yu Feng, Eric W. Moore, Jake VanderPlas, Denis Laxalde, Josef Perktold, Robert Cimrman, Ian Henriksen, E. A. Quintero, Charles R. Harris, Anne M. Archibald, Aaron H. Ribeiro, Fabian Pedregosa, Paul van Mulbregt, and SciPy 1.0 Contributors. Scipy 1.0: Fundamental algorithms for scientific computing in python. *Nature Methods*, 17:261–272, 2020.
- [51] Filippos Koliopanos, Marat Gilfanov, Lars Bildsten, and María Díaz Trigo. X-ray diagnostics of chemical composition of the accretion disc and donor star in ucxbs-ii. xmm-newton observations. *Monthly Notices of the Royal Astronomical Society*, 442(3):2817–2825, 2014.
- [52] Walter HG Lewin, Jan Van Paradijs, and Ronald E Taam. X-ray bursts. *Space Science Reviews*, 62:223–389, 1993.
- [53] Erik Kuulkers, PR i den Hartog, FWM Verbunt, William E Harris, M Cocchi, et al. Photospheric radius expansion x-ray bursts as standard candles. *Astronomy & Astrophysics*, 399(2):663–680, 2003.
- [54] HEASARC. NICER Analysis Thread: NICERL2 - Processing of Level 1 Data to Level 2. https://heasarc.gsfc.nasa.gov/docs/nicer/analysis_threads/nicerl2/, 2025. Accessed 2025.